Experimental and numerical studies on scaled-down dry-joint retaining walls: Pseudo-static approach to quantify the resistance of a dry-joint brick retaining wall

Nathanaël Savalle, Éric Vincens, Stéphane Hans

Experimental and numerical studies on scaled-down dry-joint retaining walls

Pseudo-static approach to quantify the resistance of a dry-joint brick retaining wall

Nathanaël Savalle[1] – Éric Vincens[2] – Stéphane Hans[3]

Abstract: A pseudo-static study on dry-joint brick retaining walls has been carried out as part of a preliminary work aiming at designing actual dry stone retaining walls located in seismic areas. First, scaled-down dry-joint brick retaining walls have been tilted towards failure and the influence of the wall geometry has been analysed. Then, numerical simulations have been performed using the Distinct Element Method to complement the observations made in the experimental tests. From both approaches, we found that the more slender the wall is, the less resistant to a pseudo-static action it results. Using the numerical model, it has also been found that the assemblage plays a significant role in the stability of dry-joint structures, with a particular emphasis on the critical role played by the headers. Moreover, the simulations brought to light complex features when failure is triggered in large walls.

Keywords: DEM – Earthquake engineering– Dry stone retaining walls – Bricks – Masonry

1. Introduction

Human beings have started to build dry stone masonry structures millennia ago (Kerisel, 1993) but most striking examples of these ages were erected during the Neolithic and Chalcolithic periods (4700 - 1500 B.C). Since stone is naturally present worldwide, vestiges of this heritage can be found in different countries such as "Stonehenge" in England, the "Iron Age Brochs" in Scotland (Thew et al., 2013) or for more recent structures, the "Great Zimbabwe" in Zimbabwe, the "Machu Picchu" in Peru. In France, the most emblematic dry stone structure is the "Pont du Gard" built by the Romans in the first century AD.

For a long time, stone masonry has then proven to be an efficient building technique in areas where the resource was easily accessible. In particular, dry stone retaining walls (DSRWs) have been used to stabilise slopes and to create terraces for agricultural purposes or for transportation. For example, DSRWs have been tightly involved to local agricultural economies in regions such as "Lavaux's Terraces" in Switzerland or such as the "Douro's Valley" in Portugal which are both UNESCO World Heritage. Recently, they have been considered as an economic leverage for the development of isolated territories renewing the tourism offer ("Ruta de pedra en sec", Serra de Tramuntana, Majorca Island, Spain, UNESCO).

The dry stone building technique requires a definite know-how where each stone must be carefully placed in order to ensure a long lasting interlocking of stones without the use of mortar. Moreover, dry stone masonry presents many relevant assets, compared to conventional techniques such as reinforced concrete. For example, the natural porosity of DSRWs enables water to flow through the wall. The low amount of embodied energy

[1] nathanael.savalle@ec-lyon.fr – University of Lyon – École Centrale Lyon
36 Av. Guy de Collongue 69134 Ecully Cedex – FRANCE
[2] eric.vincens@ec-lyon.fr – University of Lyon – École Centrale Lyon
36 Av. Guy de Collongue 69134 Ecully Cedex – FRANCE
[3] stephane.hans@entpe.fr – University of Lyon – École Nationale des Travaux Publics de l'État (ENTPE)
R. Maurice Audin 69518 Vaulx-en-Velin – FRANCE

required for extracting stones in quarries and for building the walls reduces the environmental impact of the retaining structures (Morel et al., 2001). Moreover, at the end of a DSRW's life cycle, more than 70% of the stones can be re-used on site.

However, decades and sometimes centuries of neglect have induced heavy damages to this valuable heritage. Repairing these structures has become an important issue for the stakeholders while there is a growing interest in prescribing this building technology as a substitute to reinforced concrete walls or gabions to preserve the quality of the landscape in territories where dry stone heritage is present.

In this context, different studies have recently been carried out to give a better insight into the mechanical behaviour of DSRWs. The first studies have been carried out in the nineteenth century (Anon, 1845; Burgoyne, 1853). Their main goal was to find the optimal shape for the section of slope DSRWs in order to maximise their resistance. Then, some authors have tried to model these experiments using Coulomb's wedge theory (Capper and Cassie, 1969; Clayton et al., 2014; Husband and Harby, 1911) following the development of this analytical method in geotechnical engineering (Heyman, 1972). Later on, other authors (Claxton et al., 2005; Harkness et al., 2000; Powrie et al., 2002) used the Distinct Element Method to simulate these experiments and to study pathologies observed in DSRWs, such as the bulging phenomenon (Powrie et al., 2002).

More recently, new experimental campaigns on full scale structures have been carried out in France in order to give some recommendations for the design of slope DSRWs (Colas et al., 2013a, 2010a; Villemus et al., 2006) while in Great Britain full scale experiments have been carried out to understand the origin of the bulging phenomenon (Mundell et al., 2010, 2009).

These experiments allowed design tools for slope DSRWs to be validated including the homogenized yield theory (Colas et al., 2008, 2013b) or other analytical methods (Alejano et al., 2012a, 2012b; Kim et al., 2011; Terrade et al., 2018).

Oetomo (2014) used different numerical approaches for the problem of DSRWs stability and compared the precision of results obtained with both analytical and numerical methods. Among these latter, we can cite the fully discrete element method (DEM) (Oetomo et al., 2016) and a mixed discrete-continuum approach (Oetomo et al., 2013) that proved to be very efficient in terms of quality of results but also in terms of computation time.

To conclude, different robust methods were able to correctly retrieve the behaviour of DSRWs observed in full-scale experiments. However, the seismic behaviour of these structures is so far unknown. Although numerous studies dealing with the stability of gravity retaining walls under seismic loading can be found in the literature only a few are taking into account the specificity of the dry stone building technique (Fukumoto et al., 2014; Savalle et al., 2018a).

The first study related to the seismic stability of retaining walls goes back in 1926 (Mononobe and Matsuo, 1929; Okabe, 1926) leading to the development of the so-called pseudo-static method also denoted Mononobe-Okabe method. Then, Newmark (1965) developed a theory to compute the displacements of retaining walls due to the seismic motion. Improving the pseudo-static approach, the pseudo-dynamic method has tried to take into account the wave propagation associated to the seismic motion (among them, Baziar et al., 2013; Bellezza, 2014; Choudhury et al., 2014). More precisely, Baziar et al. (2013) brought to light that the estimate of the seismic action using pseudo-static methods may be over-conservative reaching a value five times bigger than that issuing from a pseudo-dynamic method.

In this work (which is envisioned as a preliminary study of the seismic behaviour of slope DSRWs), scaled-down experiments involving a mock-up of a dry-joint brick wall retaining a sandy backfill that was tilted towards failure has been carried out. First, the experimental results are briefly presented. Then, a plane strain DEM numerical model that has already been proven to be relevant to model DSRWs (Claxton et al., 2005; Dickens and Walker, 1996; Harkness et al., 2000; Powrie et al., 2002; Walker et al., 2007; Walker and Dickens, 1995) is used to catch the observed experimental phenomena. Moreover, the DEM model was used to study the

failure of DSRWs more in detail, as well as the influence of the assemblage chosen to build the walls on their resistance.

2.   Experimental protocol

1.   Principle of the test

The tests consisted in tilting a scaled-down model of a dry-joint retaining wall until its collapse (*Figure 1*). In a container, a wall made of clay bricks retained a backfill made of dry Hostun sand. As the container was tilted, the pseudo-static action denoted a_h issuing from the natural gravity decomposition (*Figure 2*) increased until the collapse of the wall. All tilting tests were video-recorded and tilting angles at failure were reported.
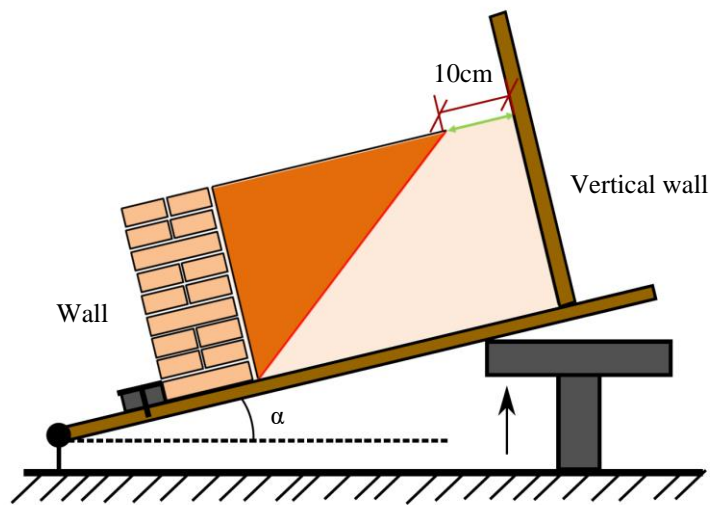

Figure 1: Cross-section view of the container and the wall-backfill system; minimum gap of 10cm between the vertical back wall of the container and the failure surface within the backfill; a piece of wood fixed to the container floor blocked the translational movement of the first row of bricks (Savalle et al., 2018a).
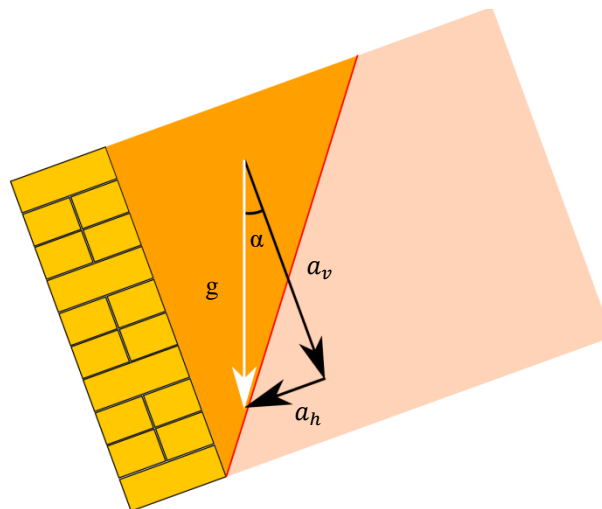
Figure 2 : Throughout the tilting test, the natural gravity is decomposed into two components: a_h perpendicular to the wall and a_v parallel to the wall (Savalle et al., 2018a).

2.   Experimental devices

The dimensions of the container were of 25cm*40cm*40cm (height H_0*width W_0*length L_0). The width dimension prevented the failure in the soil from reaching the container's wall (*Figure 1*). The wall was placed in

the aperture of the container (*Figure 3*). For all the tests, the length L of the wall was chosen large enough, and thus equal to the length L_0 to guarantee a condition of plane strain (more details about the plane strain condition can be found in Savalle et al. (2018b)). Besides, only monolithic failures occurred during the experiments and a quasi-perfect plane strain failure pattern could be observed.

The height H ranged between 34mm and 190mm while the width's range was between 34mm and 85mm leading to wall aspect ratios H/B varying from 1 to 4. The down scaling of the brick wall was approximately between $1/30^{th}$ and $1/10^{th}$ compared to actual DSRWs. It should be noted that for the sake of simplicity, the wall sections were rectangular with parallelepiped shaped bricks while actual DSRWs usually present an external batter which increases their resistance (Burgoyne, 1853; Colas et al., 2010b).
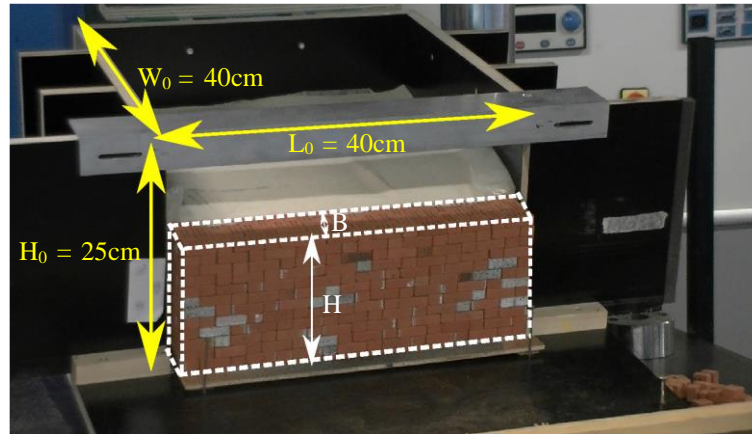

Figure 3: Scaled-down model during a test. The wall (height H and width B) is placed in the aperture of the container.

The retained backfill, made of dry Hostun sand, has been pluviated from a zero-drop height to obtain a very loose state. Some grains of sand were glued on the container floor to clarify the bottom boundary conditions. Similarly, a wood stick of 1cm height was fixed in front of and at the bottom of the wall to prevent the first row of bricks to move. Therefore, in the following, the height H of the wall refers to the height of the wall free to move (ignoring this first blocked layer). Then, the whole system was tilted using a plunge (from a hydraulic press), elevating the back of the container while the other end was maintained fixed (*Figure 3*).

The physical and the mechanical parameters of the materials involved in the experiments are summed up in *Table 1* and *Table 2*. The dimensions of the regular bricks were h*b*l = 11.5mm*17mm*34mm. More details about the brick dimensions can be found in *Appendix I*. Their unit weight was $16.0\ kN.m^{-3}$, whereas the overall unit weight of the wall (including pores) was $14.4\ kN.m^{-3}$. The friction coefficient between brick layers has been previously experimentally evaluated to $32° \pm 2°$ (Quezada et al., 2016). Hostun sand had a mean unit weight of $13.2\ kN.m^{-3}$ corresponding to a relative density R_D of 4%. The internal friction angle of the sand has been taken equal to $32°$ according to Quezada et al. (2016). The friction coefficient of the interface between the wall and the backfill has been identified during this experimental campaign (Savalle et al., 2018a). Based on eighteen tests, this friction angle has been evaluated to $22.7° \pm 2°$.

Table 1: Unit weight of the materials involved in the experiments: bricks, wall and backfill.

	Clay bricks	Wall	Hostun sand backfill
Unit weight ($kN.m^{-3}$)	16.0	14.4	13.2

Table 2: Mechanical parameters of the contact properties: bricks, backfill and interface.

	Clay bricks	Hostun sand backfill	Wall-backfill interface
Friction angle (°)	32	32	22.7
Cohesion (kPa)	0	0	0

The peculiar assemblage of blocks is the key feature of the dry stone building technique where the strong interlocking of blocks and their staggered positioning allows the DSRW to behave as a whole. Herein, an assemblage using both headers and stretchers has been used. This assemblage is close to the practice of dry stone masons (CAPEB et al., 2008; ENTPE et al., 2017). In *Figure 4*, the assemblage is detailed for the walls built with a width of B = 34mm (corresponding to the length of a single regular brick). This latter one holds slightly more horizontal joints (+50%) than vertical joints, in terms of equivalent surface. Based on the same mix of headers and stretchers, assemblages used for walls of bigger widths are detailed in *Appendix I*. A numerical study of the influence of the assemblage is then presented in the following (Section 5.2).
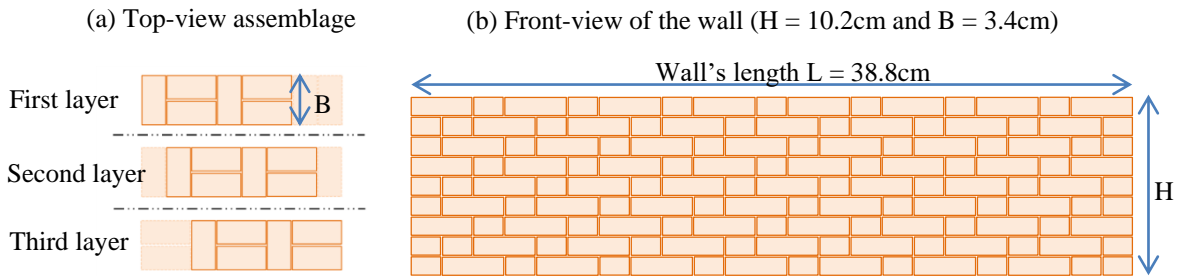
(a) Top-view assemblage   (b) Front-view of the wall (H = 10.2cm and B = 3.4cm)

Figure 4: Top (a) and front (b) views of the assemblage used to build the experimental wall of width B = 3.4cm

3.   Experimental results

The experimental campaign consisted in studying the influence of the geometrical parameters (wall height H, wall base B, and the wall aspect ratio H/B) on the tilting angle at failure. First, to better stress the natural variability of the results in the experimental tests, repeatability tests have been performed for four different walls of width B = 3.4cm having different aspect ratios (or slendernesses) H/B. For each different wall, the tilting tests have been repeated six times which led to a standard deviation for the tilting angle at failure smaller than 1°. In the following, this natural scatter of results due to the materials and to the protocol will stand as a reference for analysing the experimental tests.

Then, to have a better insight into the influence of the aspect ratio on the induced failure, ten wall geometries were tested. For convenience, they all held the same width (B = 34mm) with a varying height (from H=34mm to H=138mm). Simultaneously, additional tests have been carried out using different wall geometries having the same aspect ratio but different base widths (*Figure 5*).
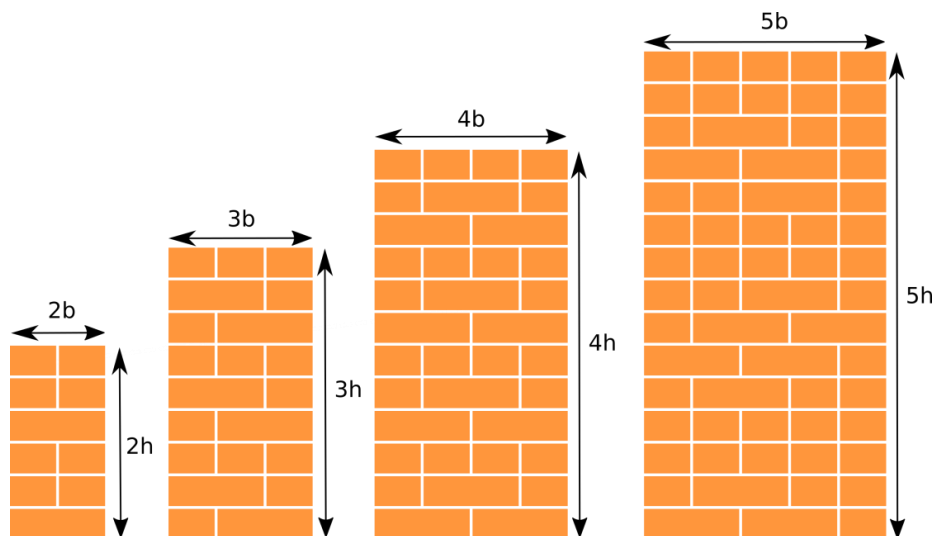

Figure 5: Section of walls having different base widths but a same aspect ratio; h and b correspond respectively to the height and the width of a single regular brick involved in the wall construction.

Table 3 sums up the dimensions of all the tested walls as well as the corresponding tilting angles at failure. The authors remind that the first layer of bricks was not supposed to move throughout the test (this feature was checked all along the experiments) and as a consequence was not included in the calculation of the height H and of the aspect ratio of the wall.

Table 3: Experimental tilting angles at failure for all tested walls. Walls are sorted according to their aspect ratio. Bold values correspond to walls with a width B of 3.4cm.

Aspect ratio (H/B)	Height (cm)	Width (cm)	Tilting angle at failure (°)
1	**3.4**	**3.4**	**24**
1.3	**4.7**	**3.4**	**20.8 (±0.8)**
1.7	**5.9**	**3.4**	**18.7**
2	**7.2**	**3.4**	**14.6**
2	10.5	5.1	14.5
2	13.6	6.8	15.5
2	17.0	8.5	13.7
2.3	**8.1**	**3.4**	**11.8**
2.7	**9.2**	**3.4**	**9.0 (±0.9)**
2.7	13.8	5.1	8.0
2.7	18.2	6.8	8.8
3	**10.4**	**3.4**	**7.9**
3.3	**11.6**	**3.4**	**4.9 (±0.4)**
3.3	17.1	5.1	4.4
3.7	**12.7**	**3.4**	**2.8 (±0.4)**
4	**13.8**	**3.4**	**1.7**

Considering the typical standard deviation of 1° for the tests, we could not find a significant influence of the base width for a given aspect ratio. The wall slenderness seems to be the key property able to explain the value of the tilting angle at failure.

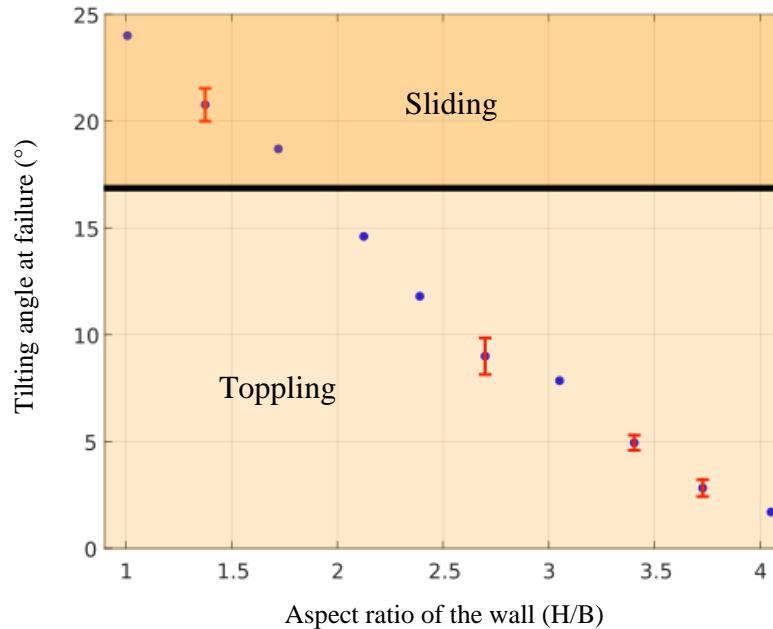*Figure 6: Experimental tilting angle at failure depending on the wall aspect ratio H/B. Base width B = 34mm; height H ∈ [35mm; 138mm] (Savalle et al., 2018a).*

Studying more specifically the influence of the aspect ratio on the induced failure, *Figure 6* draws the experimental results, as well as the typical extent of experimental results corresponding to repeatability tests. The

two typical modes of failure of dry stone structures, sliding and toppling, were experimentally retrieved. Sliding failures occurred for less slender walls while toppling/overturning failures happened for more slender walls. The transition between these two modes of failure have been found between slendernesses H/B = 1.7 and H/B = 2.05. Moreover, walls having the same slenderness collapsed following the same failure mode.

4.   Numerical modelling

A plane strain modelling of the experiments using the Distinct Element Method (UDEC, code ITASCA (Cundall and Strack, 1979)) has been used to complement the experiments. A validation of the numerical model is first proposed based on the tested walls. Then, particular patterns concerning the modes of failure of DSRWs are described.

1.   Basic aspects of UDEC

UDEC is a plane strain DEM code that allows a simple modelling of discontinuities where blocks can be defined either as rigid or deformable bodies. Blocks interact one with another at contacts, also called joints. In the past, it has been used in different studies involving the modelling of DSRWs (Claxton et al., 2005; Harkness et al., 2000; Oetomo et al., 2013; Powrie et al., 2002; Walker et al., 2007). In the light of these past studies on 3D drystone structures, UDEC was used to model the experiments reported in *Section 3*.

2.   Modelling procedure of the experiments

In this work, the backfill was modelled as a single deformable block. Likewise, each brick was modelled as a distinct deformable block. The contact laws between bricks followed a Mohr-Coulomb slip model.

The numerical model is presented in *Figure 7*. To reduce the computational costs, the mesh size in the backfill was increased as the distance with the inward wall face increased. The stiffnesses of the interfaces between these differently meshed blocks should be higher than (UDEC manual: Itasca, 2011):

$$k_{n,min} = k_{s,min} = 10 * \frac{K + \frac{4}{3}G}{\Delta_{z,min}} \qquad \textit{(Eq. 1)}$$

where K and G are respectively the bulk and shear moduli of the backfill and $\Delta_{z,min}$ is the width of the smallest element linked to this interface. This formula has also been used by other authors for their numerical simulations (Marino et al., 2017; Zamiran and Osouli, 2018).
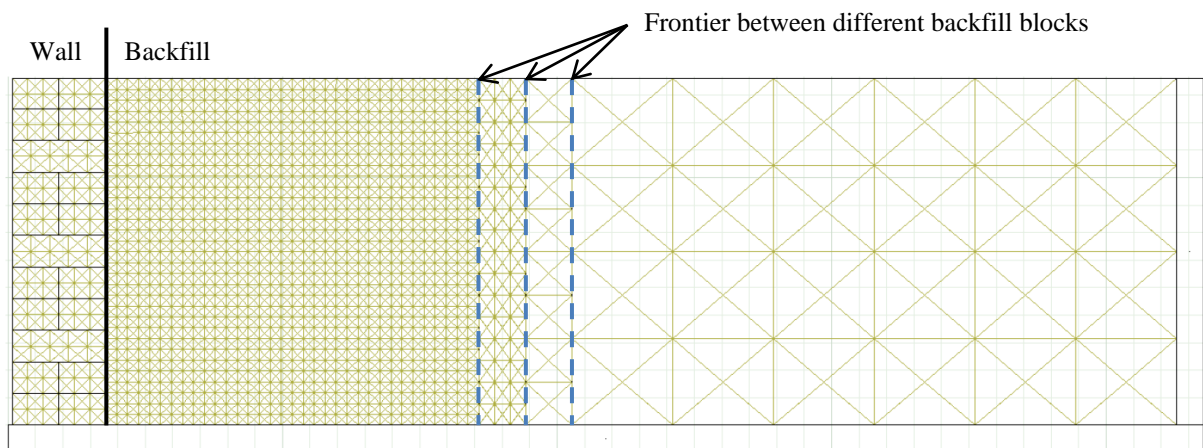

Figure 7: Modelled system: cross-section view. The thick black line represents the backfill-wall interface. Different mesh sizes were used for the backfill.

In this work, the stability of the wall was first computed, until the model reached the static equilibrium, characterised by an unbalanced force ratio smaller than 10^{-5}. Then, the backfill was activated and a new equilibrium for the backfill-wall system was computed. Finally, the modelling of the tilting movement was obtained by incrementally modifying the orientation of the gravity (increment of 0.1°) until the wall reached failure. Failure was stated based on an energy criterion similar to the one used by Oetomo, (2014), which is described in the following paragraph.

After each stage of 3000 computational increments, the total kinetic energy of the wall was computed from the energy of each block, separating the contribution of the translational kinetic energy from the rotational kinetic energy. The wall was qualified as stable when its total kinetic energy was lower than a critical threshold $E_{c,min}$ during five consecutive stages. If the wall was stable, the gravity was inclined for a further 0.1° before stability was checked again. Given a gravity inclination, the wall was qualified as unstable when its total kinetic energy exceeded another critical threshold, denoted $E_{c,max}$ during 200 increments which were not necessarily consecutive and failure was supposed to have been reached.

Finally, a complete simulation lasted approximately four hours on a HP computer of 2.3GHz speed. However, for some simulations, larger computational time, up to one day, were needed depending on the wall failure pattern.

3. Model parameters

1. Joint and material properties

Table 4 (resp. *Table 5*) gathers all the volume element (resp. joint element) properties required for the numerical simulations. The unit weight used for the bricks was identified so that the wall density was equal to the one existing in the experiments. The bricks were modelled as fully elastic as failure surface was supposed to follow the joints. The backfill was assumed to follow a Hooke's law, with parameters drawn from a previously similar numerical 3D study (Quezada et al., 2016). Plasticity in the backfill follows a Mohr-Coulomb's law.

Table 4: Volume element properties of the wall and of the backfill.

	Clay bricks	Hostun sand backfill
Unit weight ($kN.m^{-3}$)	14.4	13.2
Friction angle (°)	-	32
Cohesion (kPa)	-	0
Dilation angle (°)	-	0
Bulk modulus K (MPa)	5.56×10^8	8.33×10^6
Shear modulus G (MPa)	4.17×10^8	3.85×10^6

Table 5: Joint element properties of the wall, backfill and interface

	Clay bricks	Hostun sand backfill	Wall-backfill interface
Friction angle (°)	32	32	22.7
Cohesion (kPa)	0	0	0
Dilation angle (°)	0	0	0
Normal stiffness k_n (Pa/m)	5×10^{12}	1×10^{11}	1×10^{11}
Tangential stiffness k_s (Pa/m)	5×10^{12}	1×10^{11}	1×10^{11}

The purely frictional joints followed a Coulomb slip model and no dilation was taken into account. Indeed, as the sand was in a very loose state, the dilation angle was equal to 0. Since in the experiments, the bricks were ideal parallelepipeds, no dilation was taken into account in the brick joints.[4] The values of the joint stiffnesses were chosen high enough not to impact the quality of the numerical simulations (following *Eq. 1*). For the special case

---

[4] In fact, some preliminary studies showed that there was not any significant influence of the dilation value on the results.

of the wall-backfill joint where the joint connected two different materials, the moduli to consider are the ones of the softer material. A parametric study involving a possible influence of the elastic properties of the joints (as well as of the materials) on the results is presented in Appendix III.

2. Numerical parameters

In order to ensure the independence of the results with respect to the mesh size a sensitivity analysis of the mesh on the tilting angle at failure was performed on a particular wall of height H=8.1cm and of width B=3.4cm. As shown in *Figure 8*, six identical numerical tests were carried out with different mesh sizes. As the refinement of the mesh increases, the tilting angle at failure is getting more stable.
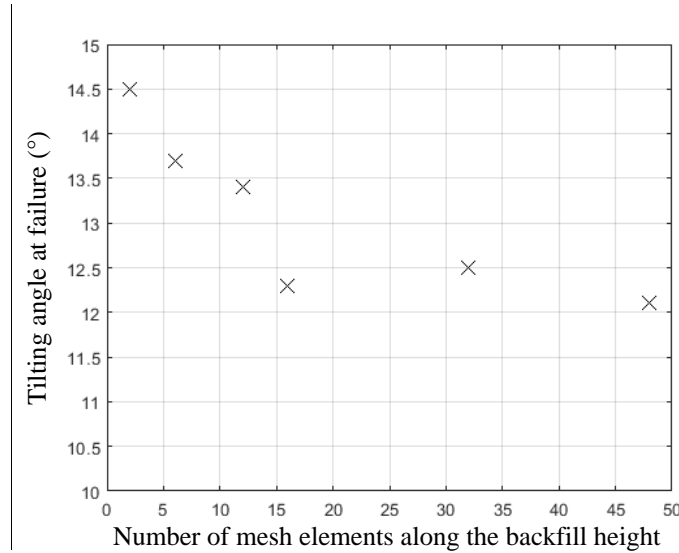

Figure 8: Influence of the refinement of the mesh size on the numerical tilting angle at failure.

A specific study has been carried out to define the energy thresholds (Section 4.2**Erreur ! Source du renvoi introuvable.**). We denote H_0 and B_0 the respective height and base width of the studied wall. A value of $E_{c,min} = 10^{-12}J$ was selected for a satisfying minimal threshold characterising stability and a value of $E_{c,max} = 10^{-10}J$ has been found relevant to characterise a system bound to collapse. For other wall geometries (H and B), the authors proposed a method to define these threshold values in *Appendix II*. It leads to the following equations:

$$E_{c,min}(H,B) = \frac{H \times B}{H_0 \times B_0} \times E_{c,min}(H_0,B_0) = \frac{H \times B}{8.1 \times 3.4} \times 10^{-12}J \qquad (Eq.\ 2)$$

$$E_{c,max}(H,B) = \frac{H \times B}{H_0 \times B_0} \times E_{c,max}(H_0,B_0) = \frac{H \times B}{8.1 \times 3.4} \times 10^{-10}J \qquad (Eq.\ 3)$$

An additional local damping of 5% was added to stabilize the numerical simulations (Kamai and Hatzor, 2008; Oetomo, 2014; Quezada et al., 2016). This value is rather small for a static study but higher values showed a tendency to mask the minimal inclination angle leading the system to an unstable state and then to failure.

4. Wall cross-section

The actual walls were built with a staggered positioning of bricks and an alternate use of stretchers and headers. It implies that depending on the location of the vertical cross-section, the assemblage included in different cross-sections could show a different pattern. This aspect does not exist for actual walls made of actual stones where some randomness of the block location and sizes (but satisfying the pattern of staggered headers and stretchers placement) tends to homogenized the behaviour of the wall. The problem arises at the moment of modelling the 3D system exhibiting some periodic patterns using a plane strain code and the relevant cross-section able to model the features observed in the experiments.

To answer this issue, a case study was analysed more in detail where four possible different patterns were identified depending on the chosen vertical cross-section. The minimal (fundamental) patterns that repeated vertically in the four different cross-sections are given in *Figure 9*.

Two different wall-backfill systems, corresponding to the two first different repeated patterns (cross-sections 1 and 2 in *Figure 9*), have been simulated with a wall having dimensions H=8.1cm and B = 3.4cm. The tilting angles at failure were found respectively equal to 12.3° and 14.4° for cross-section 1 and 2; this difference is not negligible. Considering walls with larger widths (5.1, 6.8 and 8.5cm) where the assemblages were more complex, this absolute difference arose 6.6°, which is very significant.
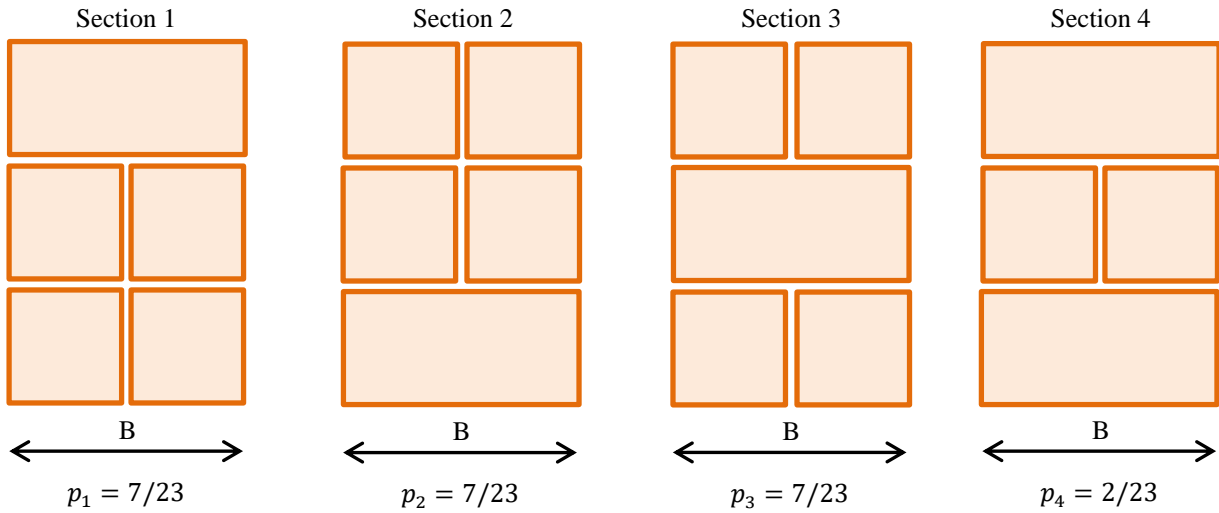

Section 1	Section 2	Section 3	Section 4
B	B	B	B
$p_1 = 7/23$	$p_2 = 7/23$	$p_3 = 7/23$	$p_4 = 2/23$

Figure 9: Four different patterns in four different vertical cross-sections (B=34mm). The three first ones were equally represented along the wall in the length. The fourth pattern corresponds to the two wall ends.

Then, to take into account a possible bias in the analysis due to the choice of the simulated cross-section, the authors proposed to derive the final tilting angle α_{mean} at failure for a wall based on simulations carried out with all the possible cross-section patterns. The final tilting angle at failure was obtained through a weighted contribution of the different tilting angles at failure obtained throughout each simulation. The weighted coefficients were related to the occurrence of a given pattern in the wall. For the case of the wall with a 3.4cm width, it reads:

$$\alpha_{mean} = p_1\alpha_1 + p_2\alpha_2 + p_3\alpha_3 + p_4\alpha_4 \qquad \text{(Eq. 4)}$$

where α_i is the tilting angle at failure associated with pattern i and p_i the proportion of pattern i along the length of the wall. In the case of the wall of width B=34mm, these proportions were: $p_1 = p_2 = p_3 = 7/23$ and $p_4 = 2/23$ (*Figure 9*).The same scheme has been applied for the walls with larger widths (51, 68 and 85mm) based on the assemblages given in *Appendix I*. Seven different patterns were identified for walls of width B = 51mm, four patterns for walls of width B = 68mm and eighteen patterns for walls of width 85mm. One should note that the proposed formula *(Eq. 4)* is a simplified approach that can be questioned. Indeed, in actual walls, the patterns are intimately interlocked one with another, which is not the case considering this numerical procedure. Moreover, if the longitudinal heterogeneity was accounted for in this study, the influence of the transversal heterogeneity was not addressed in detail (especially for non-symmetrical assemblages in cross-sections).

5. Numerical results

This section is devoted to the validation of the numerical tool and to its use on a special case study of the assemblage of dry-joint walls.

1. Simulation of the experiments

Using the experimental campaign developed in *Section 3*, a numerical modelling of the tilting tests has been carried out to study the influence of the slenderness on the tilting angle at failure. Ten walls of a same width (34mm) and various heights were simulated (using for each one the four different possible patterns in the cross-sections according to *Section 4.4*) and the mean tilting angle at failure was computed using *(Eq. 4*.

Figure 10 gives the results of the simulations together with the results found through the experiments. The maximum departure between the experimental results and the simulations is of 1.7° which corresponds to a relative difference of 13%. It is close to the natural dispersion of the experimental results of 1°.
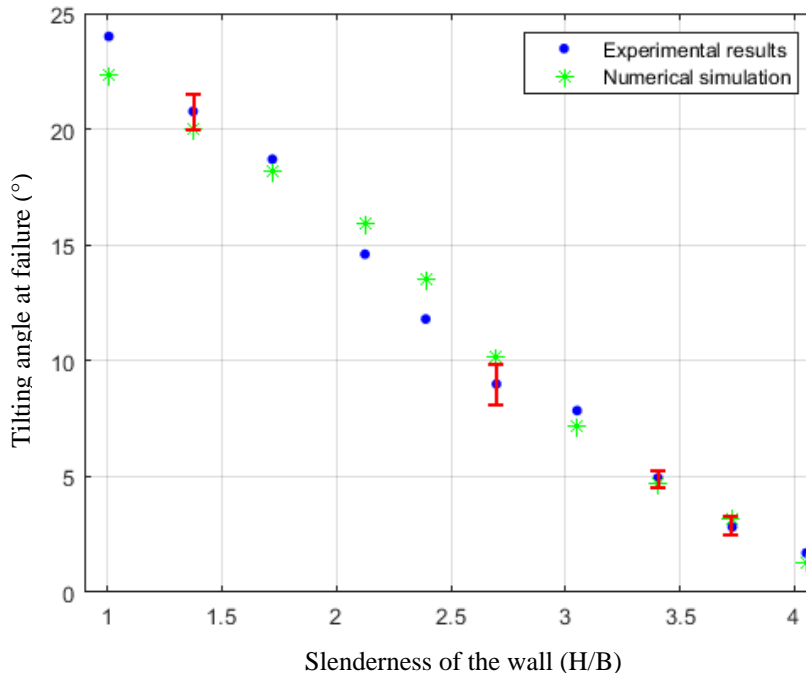

Figure 10: Comparison between the tilting angles at failure obtained through experiments and simulations. Influence of the wall slenderness.

Globally, the numerical model has been found in a good agreement with the experimental results. The observed departure can arise from experimental scattering as well as numerical assumptions of the modelling procedure (statement of stability of the wall, weight ponderation to compute the tilting angle, plane strain assumption). Moreover, the different modes of failure were correctly retrieved. In the simulations, the less slender walls failed by sliding (*Figure 11*), while the more slender walls failed by overturning (*Figure 12*).

In the sliding mode of failure, the whole wall moved with approximately the same velocity (*Figure 11*). On the contrary, the toppling mode of failure was characterised by a triangular velocity field in the wall, with the higher velocities at the top of it. Moreover, a part of the wall, located at the bottom right corner of it, remained stable and did not move (*Figure 12*). This pattern is close to the one obtained by de Felice (2011) in his simulations involving masonry walls subjected to out-of-plane loading. The transition between these two failure modes has been evaluated to take place approximately for walls with a slenderness of H/B = 2.0 which is very close to the value H/B = 1.9 found throughout the experiments. Indeed, for this particular case (slenderness H/B = 2.0), both sliding and overturning have been observed in the numerical simulations depending on the pattern of the cross-section considered in the simulation. *Figure 12* gives the velocity field at failure for wall (H = 7cm and B = 3.4cm) with a pattern corresponding to cross-section 1 and *Figure 11* gives this velocity field for a wall with a pattern corresponding to cross-section 4 (*Figure 9*).
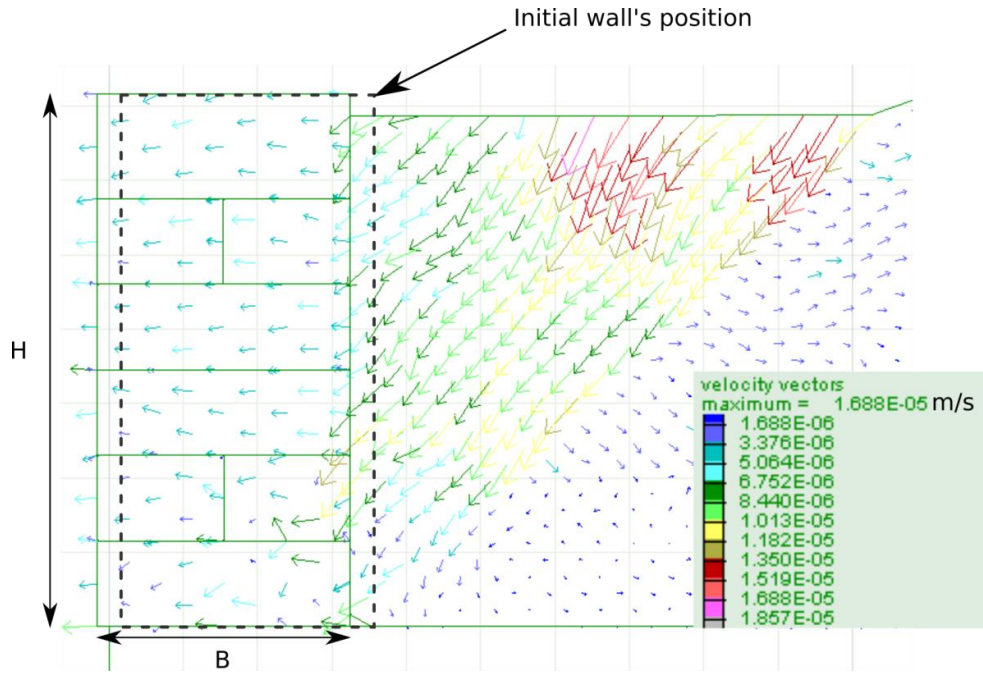
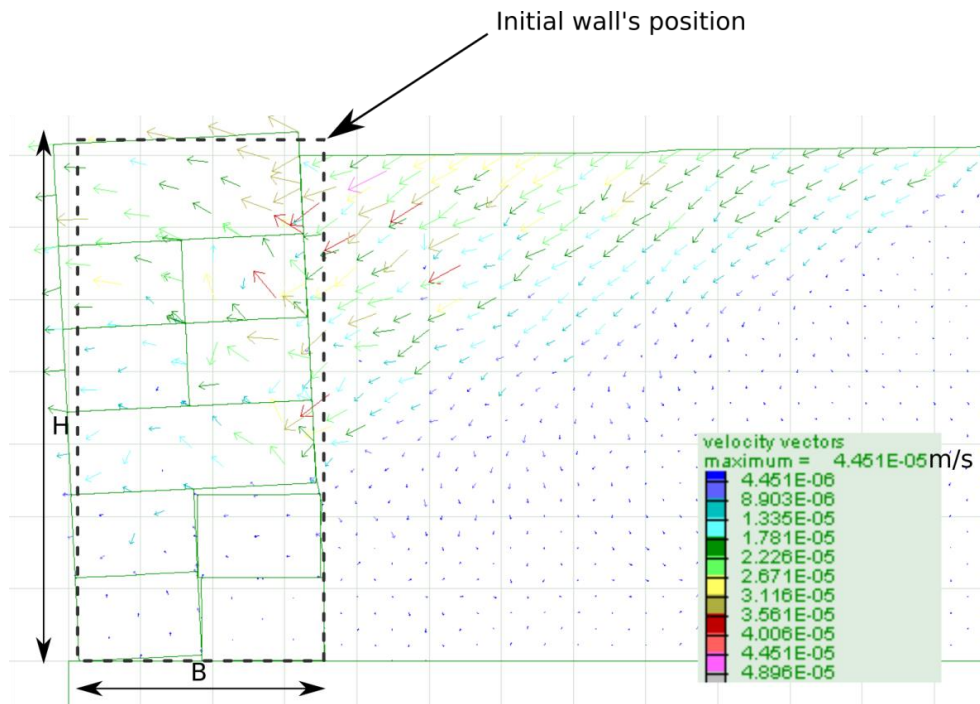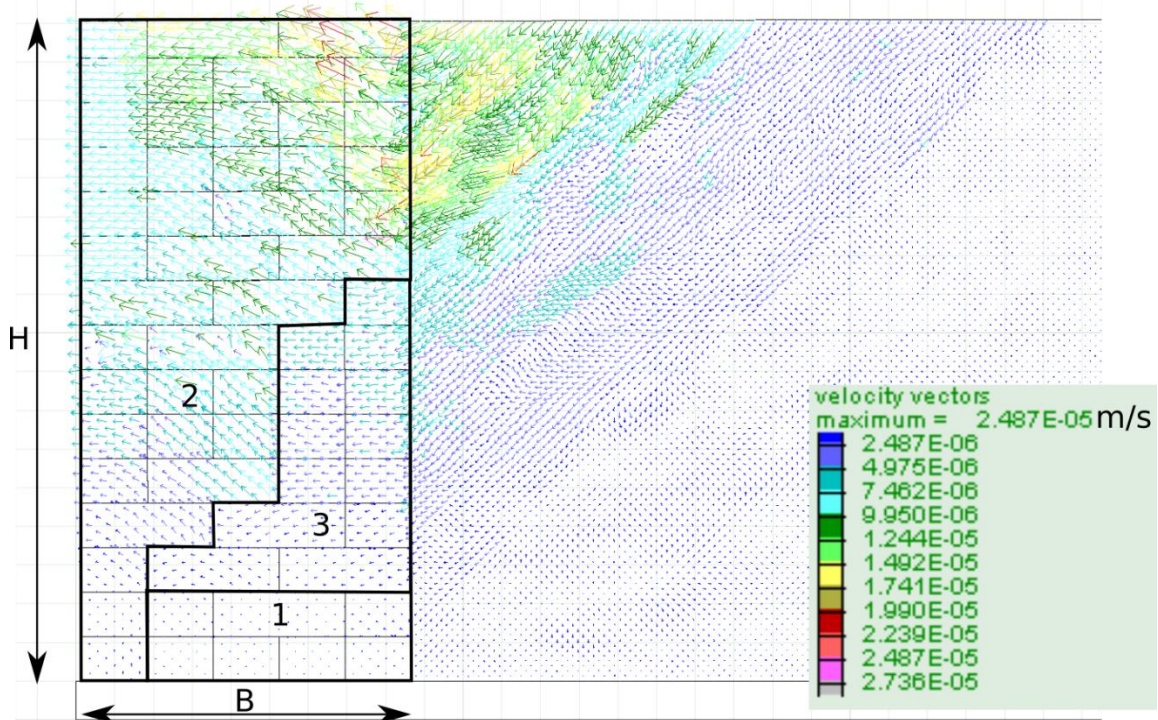*Figure 11: Velocity field (wall: H/B = 2, cross-section 4) at failure: sliding mode.*

Figure 12: Velocity field (wall: H/B = 2, cross-section 1) at failure: toppling mode.

Moreover, the numerical model has been tested on the experiments carried out on walls with identical aspect ratios but bigger widths (*Section 3*). Numerical and experimental tilting angles at failure are compared together in *Table 6*. The deviations between simulations and experiments are small. Then, it tends to validate the method proposed in *Section 4.4*, which provides a useful method for the simulation of the mechanical behaviour of dry-joint masonry when a representative cross-section is difficult to extract for a plane strain simulation.

Table 6: Numerical and experimental wall tilting angles at failure for the same slenderness.

Aspect ratio (H/B)	Height (cm)	Experimental tilting angle (°)	Numerical tilting angle (°)
2	7.2cm	14.6°	15.9°
	10.5cm	14.5°	14.7°
	13.6cm	15.5°	16.3°
	17.0cm	13.7°	13.9°
2.7	9.1cm	9.0°	10.2°
	13.8cm	8.0°	10.1°
	18.2cm	8.8°	8.7°
3.3	11.6cm	4.9°	4.7°
	17.1cm	4.4°	6.5°

Analysing the failure of the thicker walls, both sliding and toppling collapses were observed as previously mentioned. However, another failure mode has been noted (*Figure 13*): this latter one is characterised by two failure lines crossing the wall dividing it into three different parts. One is stable (zone labelled 1 on *Figure 13*) at bottom right of the wall; another is overturning (zone 2 on *Figure 13*) at top left part of the wall. For the last part at mid-height right of the wall (zone 3 on *Figure 13*) it seems that a sliding mode of failure is processing. This feature may appear for walls built with small blocks compared to the wall thickness: a mean of four blocks in the wall thickness may be required to observe such phenomenon. This last point emphasizes the relevance of numerical models (as well as experiments) to understand the failure modes of DSRWs.

Figure 13: Velocity field (wall: B=85mm, cross-section 10). Three different kinematic patterns in the wall can be observed.

2. Influence of the assemblage

As noted before, the peculiar assemblage of blocks is a key feature of the dry stone building technique. In this subsection, the numerical model is used to study the influence of the assemblage on the numerical tilting angle at failure, and particularly the importance of headers. Three particular assemblages (with the associated 2D cross-sections) were investigated (*Figure 14*). Case (a) corresponds to a fully header assemblage; case (b) to a fully stretcher assemblage which is typical of conventional bonded masonry; and case (c) to the assemblage used for the experiments as well as the numerical simulations of the previous subsection.

N. Savalle, E. Vincens, S. Hans (2019)

The plane strain numerical model has been used to simulate the tilting angle at failure of a wall of dimension H = 9.1cm and B = 34mm depending on the assemblages (a), (b) and (c). For the simulation of case (a) and (b), all cross-sections were identical all along the length of the wall. For these cases, only one simulation was required, contrary to case (c) (*Section 4.4*). The results are given in *Table 7*. Headers seem to greatly improve the resistance of dry-joint retaining walls as it has already been noted by Giuffrè (1996), de Felice (2011) and Pulatsu et al, (2016) (among others) for masonry walls subjected to out-of-plane loading.
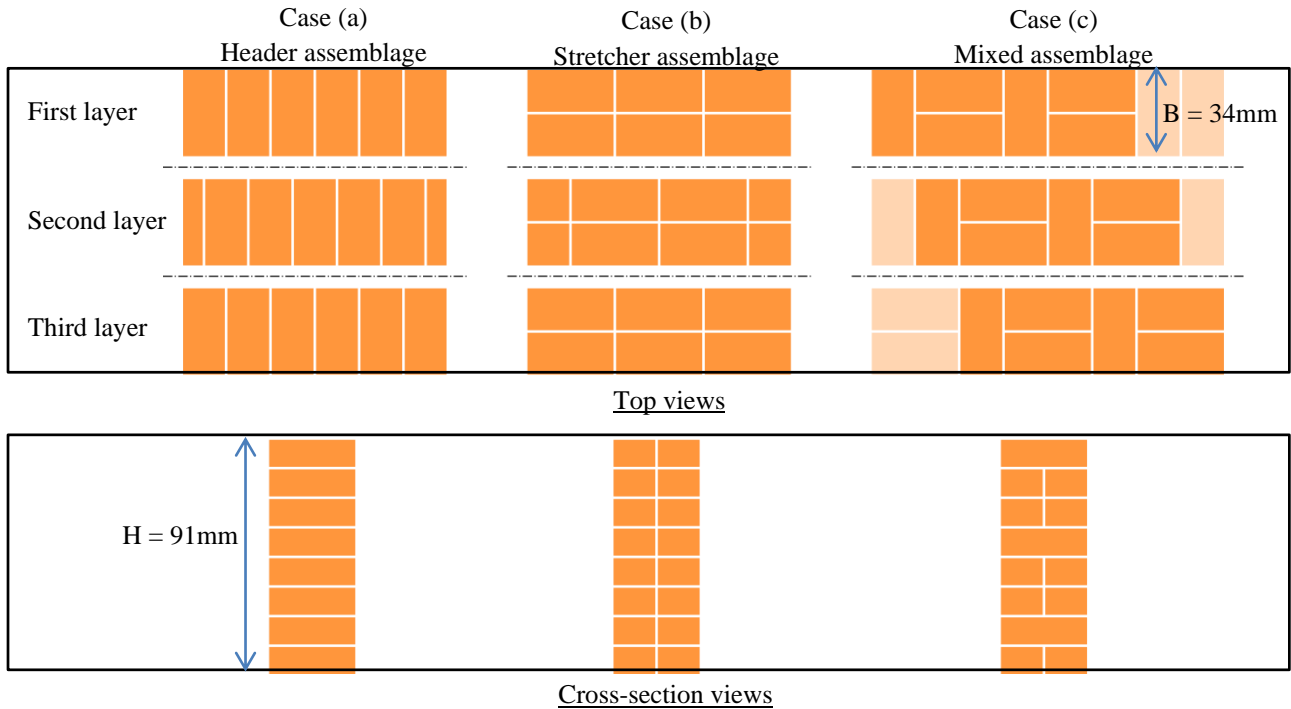

Figure 14: Top and cross-section views of different assemblages used for the numerical study. (a) Header assemblage. (b) Stretcher assemblage. (c) Mixed assemblage (the one used in the experiments, Figure 4).

Table 7: Numerical simulations of the tilting angles at failure according to different assemblages (Figure 14).

	Case (a) Header assemblage	Case (b) Stretcher assemblage	Case (c) Mixed assemblage
Tilting angle at failure (°)	11.5°	4.8°	10.2°

Moreover, studying more specifically the failure modes of some particular simulations made with B=85mm (*Section 5.1*), local failures due to a lack of headers were noticeable (*Figure 15*). It has a practical consequence for DSRWs construction: attention must be paid to the headers at wall top which help to the stabilisation of the upper part of the wall. All these observations are in agreement with the practise of dry-stone masons who try to put as much headers as possible in the walls. However, enough long stones are rare in practise and stretchers are also needed to ensure a maximum number of contacts between stones. This is why case (c) is the most representative assemblage of actual DSRWs. According to *Table 7*, case (c) is strongly more resistant than case (b) and only slightly less resistant than case (a), which means that only adding some headers (which is the case in practise) is enough to improve significantly the resistance of DSRWs. This last comment is in accordance with the results of de Felice, (2011) who showed that adding only 7% of through-headers in a masonry wall increased a lot its seismic out-of-plane ultimate capacity and that adding more headers only slightly improved its resistance. A subsidiary conclusion is that building dry-stone as conventional masonry (case (b) fully stretcher assemblage) will lead to extremely weak structures.
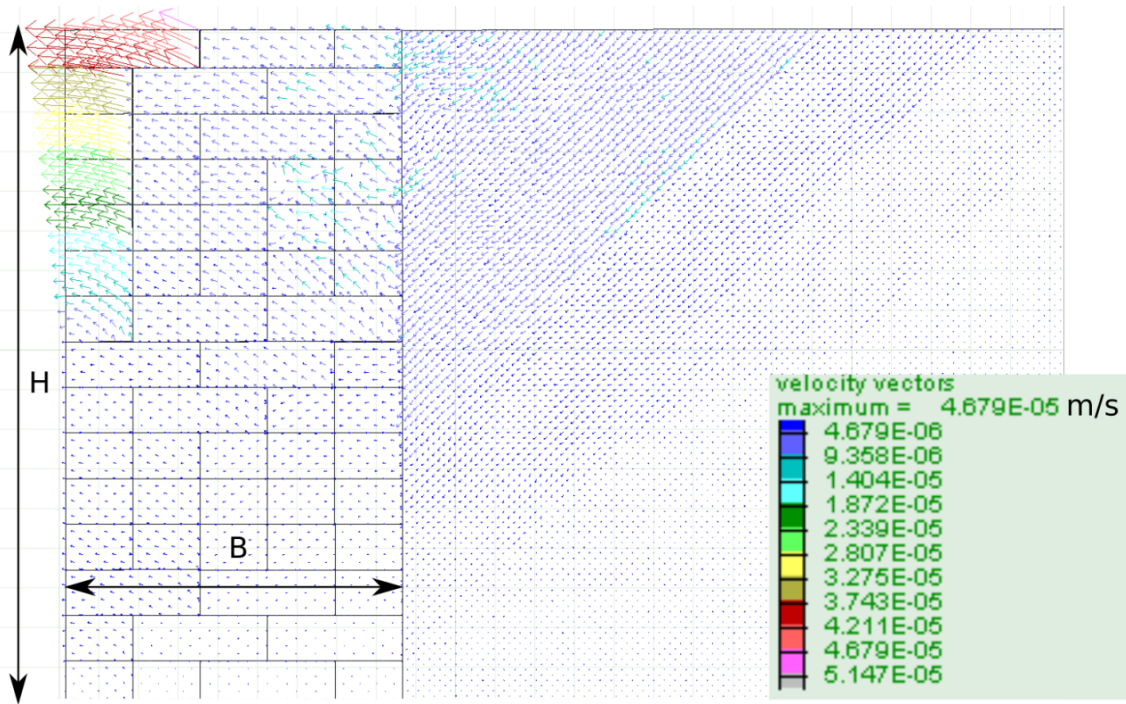
Figure 15: Velocity field exhibiting a local failure at wall top (B = 85mm).

3. Discussion about the practical use of the numerical tool

The efficiency of the numerical tool may be questionable considering the time required for a single simulation[5]. Comparing experimental results, numerical and analytical simulations (Savalle et al., 2018a) on *Figure 16*, it appears that the numerical model does not fit the experiments better than the previously developed analytical method.
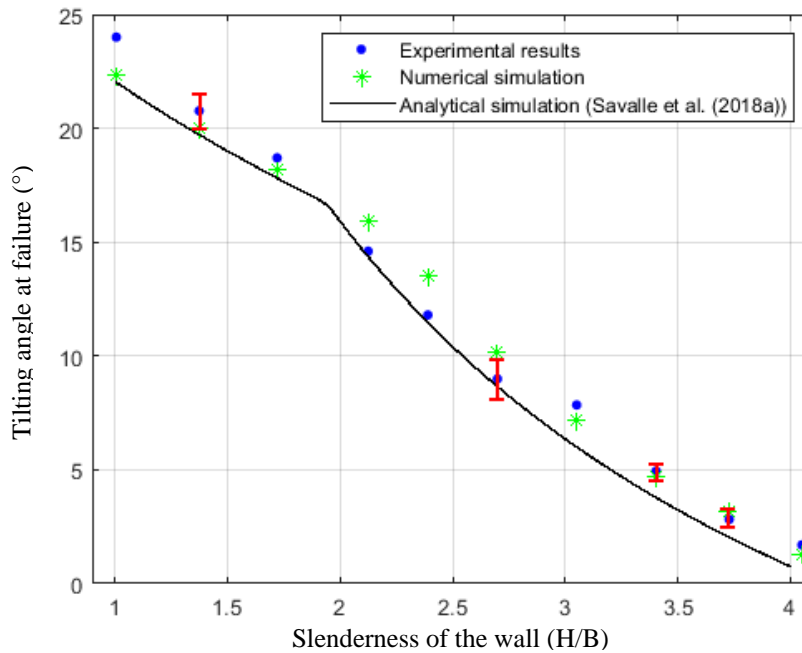

Figure 16: Comparison between the numerical simulation and the analytical simulation of Savalle et al., 2018a.

---

[5] In fact, faster simulations lasted 40 minutes; common simulations lasted 1h30 and particular simulations lasted almost one day which made skyrocketed the mean duration of a simulation.

However, the numerical DEM plane strain code has been useful to emphasize the importance of headers in a dry-joint (and thus dry-stone) retaining wall. This code also gives more details about the failure mechanisms, as well as the time evolution of the system towards failure. Moreover, it may be very helpful at the time when detailed case studies are carried out.

Considering, the quality of the plane strain numerical simulations, fully 3D DEM numerical model is not expected to give much more precise results (in terms of tilting angle at failure). A comparison between 3D and plane strain DEM code should emphasize this last point. Moreover, FEM simulations (provided that FEM models include a damage model to enable the localisation of strain in the wall) seem to be practicable since the displacements/velocities of elements are rather small according to *Figure 11-Figure 12Figure 13* and *Figure 15*.

6. Conclusion

A pseudo-static study on dry-joint retaining walls has been presented in this paper, as part of a preliminary study to address the seismic behaviour of actual DSRWs. Scaled-down experiments on dry-joint retaining walls have been carried out to have more insight into the basic aspects of dry-joint retaining wall behaviour. The tilting tests that were performed allowed quantifying the wall resistance where the less slender walls tended to collapse according to a sliding mode of failure whereas the more slender walls collapsed according to a toppling mode.

In a second part, plane strain DEM simulations have been carried out to complement the experiments. The simulations of the tilting tests have been found successful to quantitatively retrieve the experimental behaviour found for the investigated dry-joint retaining walls. In particular, the slenderness for which the failure mode changes from sliding to toppling was correctly retrieved. However, in the context of this study, no more precise results were obtained compared to a limit analysis approach, showing that analytical methods are completely relevant for design purposes.

Numerical study also pointed out the importance of headers in dry-joint retaining walls and by extension in actual DSRWs that enable the wall made of individual blocks to behave as a whole. Furthermore, numerical simulations brought to light peculiar situations where both patterns related to a toppling and sliding modes of failure take place in different zones of a same wall. Given the quality of the numerical results, the methodology proposed to study dry-joint structures was validated, and especially the energy failure criteria. In the case where some periodicity of assemblages with idealized identical blocks may exist in the wall a weighted formula including the resistance of each cross-section was proposed to derive the correct tilting angle at failure and was validated. The weighting coefficients are related to the occurrence of a given assemblage along the wall length.

In the future, true dynamic computations are envisioned to address the cases when the pseudo-static method is no more valid. It corresponds to conditions where the equivalent inertial forces involved in the pseudo-static method are associated to motions existing in average and high seismic areas.

References

Alejano, L.R., Veiga, M., Gómez-Márquez, I., Taboada, J., 2012a. Stability of granite drystone masonry retaining walls: II. Relevant parameters and analytical and numerical studies of real walls. Géotechnique 62, 1027–1040.

Alejano, L.R., Veiga, M., Taboada, J., Díez-Farto, M., 2012b. Stability of granite drystone masonry retaining walls: I. Analytical design. Géotechnique 62, 1013 –1025.

Anon, 1845. Experiments carried on at Chatham by the late Lieutenant Hope, Royal Engineers, on the pressure of earth against revetments, and the best form of retaining walls. Corps R. Eng. 7, 64–86.

Baziar, M.H., Shahnazari, H., Moghadam, M.R., 2013. Sliding stability analysis of gravity retaining walls using the pseudo-dynamic method. Geotech. Eng. 166, 389–398.

Bellezza, I., 2014. A New Pseudo-dynamic Approach for Seismic Active Soil Thrust. Geotech. Geol. Eng. 32, 561–576. https://doi.org/10.1007/s10706-014-9734-y

Burgoyne, J., 1853. Revetments of retaining walls. Corps R. Eng. Pap. 3, 154–159.

CAPEB, ABPS, Muraillers de Provence, CBPS, CMA84, ENTPE, 2008. Pierres sèches : guide de bonnes pratiques de construction de murs de soutènement. ENTPE.

Capper, P.L., Cassie, W.F., 1969. The mechanics of engineering soils. The national academy of science engineering medicine.

Choudhury, D., Katdare, A.D., Pain, A., 2014. New Method to Compute Seismic Active Earth Pressure on Retaining Wall Considering Seismic Waves. Geotech. Geol. Eng. 32, 391–402. https://doi.org/10.1007/s10706-013-9721-8

Claxton, M., Hart, R.A., McCombie, P.F., Walker, P.J., 2005. Rigid block distinct-element modelling of dry-stone retaining walls in plane strain. ASCE J. Geotech. Geoenvironmental Eng. 131, 381–389.

Clayton, C.R., Woods, R.I., Bond, A.J., Milititsky, J., 2014. Earth pressure and earth-retaining structures. CRC Press.

Colas, A.-S., Morel, J.-C., Garnier, D., 2013a. Assessing the two-dimensional behaviour of drystone retaining walls by full-scale experiments and yield design simulation. Géotechnique 63, 107–117.

Colas, A.-S., Morel, J.-C., Garnier, D., 2013b. Yield design modelling of dry joint retaining structures. Constr. Build. Mater. 41, 912–917.

Colas, A.-S., Morel, J.-C., Garnier, D., 2010a. Full-scale field trials to assess dry-stone retaining wall stability. Eng. Struct. 32, 1215–1222.

Colas, A.-S., Morel, J.-C., Garnier, D., 2010b. 2D modelling of a dry joint masonry wall retaining a pulverulent backfill. Int. J. Numer. Anal. Methods Geomech. 34, 1237–1249.

Colas, A.-S., Morel, J.-*C, Garnier, D., 2008. Yield design of dry-stone masonry retaining structures - Comparisons with analytical, numerical, and experimental data. Int. J. Numer. Anal. Methods Geomech. 32, 1817–1832.

Cundall, P.A., Strack, O.D.L., 1979. A discrete numerical model for granular assemblies. Géotechnique 29, 47 –65.

de Felice, G., 2011. Out-of-plane seismic capacity of masonry depending on wall section morphology. Int. J. Archit. Herit. 5, 466–482.

Dickens, J.G., Walker, P.J., 1996. Use of distinct element model to simulate behaviour of dry-stone walls. Struct. Eng. Rev. 2–3, 187–199. https://doi.org/10.1016/0952-5807(95)00059-3

ENTPE, Artisans Bâtisseurs en Pierre Sèche (ABPS), Ecole des Ponts ParisTech, IFSTTAR, Fédération Française du Bâtiment (FFB), 2017. Technique de construction des murs en pierre sèche : Règles professionnelles. ENTPE, Artisans Bâtisseurs en Pierre Sèche (ABPS).

Fukumoto, Y., Yoshida, J., Sakaguchi, H., Murakami, A., 2014. The effects of block shape on the seismic behavior of dry-stone masonry retaining walls: A numerical investigation by discrete element modeling. Soils Found. 54, 1117–1126.

Giuffrè, A., 1996. A mechanical model for statics and dynamics of historical masonry buildings, in: Protection of the Architectural Heritage against Earthquakes. Springer, pp. 71–152.

Harkness, R.M., Powrie, W., Zhang, X., Brady, K.C., M.P. O'Reilly, 2000. Numerical modelling of full-scale tests on drystone masonry retaining walls. Géotechnique 50, 165–179.

Heyman, J., 1972. Coulomb's memoir on statics: an essay in the history of civil engineering. CUP Archive.

Husband, J., Harby, W., 1911. Structural engineering. Longmans, Green, and Company.

Itasca, 2011. Universal Distinct Element Code (UDEC) : Theory and background, 5th Edition. Itasca Consulting Group.

Kamai, R., Hatzor, Y.H., 2008. Numerical analysis of block stone displacements in ancient masonry structures: A new method to estimate historic ground motions. Int. J. Numer. Anal. Methods Geomech. 32, 1321–1340.

Kerisel, J., 1993. History of retaining wall design, in: RETAINING STRUCTURES. PROCEEDINGS OF THE CONFERENCE ORGANIZED BY THE INSTITUTION OF CIVIL ENGINEERS AND HELD ON 20-23 JULY, 1992 AT ROBINSON COLLEGE, CAMBRIDGE.

Kim, S.-S., Mok, Y.-J., Jung, Y.-H., 2011. Behavior of dry-stone segmental retaining wall using physical modeling and numerical simulation. J. Korean Geotech. Soc. 27, 25–36.

Marino, G., Osouli, A., Zamiran, S., Shafii, I., 2017. Performance of a pier group foundation in swelling rock. Geotech. Geol. Eng. 35, 91–109.

Mononobe, N., Matsuo, H., 1929. On the Determination of Earth Pressures during Earthquakes, in: World Engineering Conference. p. 176.

Morel, J.C., Meshbah, A., Oggero, M., Walker, P., 2001. Building houses with local materials: means to drastically reduce the environmental impact of construction. Build. Environ. 36, 1119–1126.

Mundell, C., McCombie, P., Bailey, C., Heath, A., Walker, P., 2009. Limit-equilibrium assessment of drystone retaining structures. Proc. Inst. Civ. Eng. Geotech. Eng. 162, 203–212.

Mundell, C., McCombie, P., Heath, A., Harkness, J., 2010. Behaviour of drystone retaining structures. Proc. Inst. Civ. Eng. Struct. Build. 163, 3–12.

Newmark, N.M., 1965. Effects of earthquakes on dams and embankments. Geotechnique 15, 139–160.

Oetomo, J.J., 2014. Comportement à la rupture des murs de soutènement en pierre sèche : une modélisation par approche discrète (PhD Thesis). Ecole Centrale de LyonI.

Oetomo, J.J., Vincens, E., Dedecker, F., Morel, J.-C., 2016. Modeling the 2D behavior of dry-stone retaining walls by a fully discrete element method. Int. J. Numer. Anal. Methods Geomech. 40, 1099–1120.

Oetomo, J.J., Vincens, E., Dedecker, F., Morel, J.C., 2013. Modeling the Two-Dimensional Failure of Dry-Stone Retaining Wall, in: Pietruszczak, S., Pande, G.N. (Eds.), Proceedings of Computational Geomechanics (ComGeo) III, Krakow, Poland. International Centre for Computational Engineering (IC2E), pp. 717–725.

Okabe, S., 1926. General Theory of Earth Pressure. J. Jpn. Soc. Civ. Eng. 12.

Powrie, W., Harkness, R.M., Zhang, X., Bush, D.I., 2002. Deformation and failure modes of drystone retaining walls. Géotechnique 52, 435–446.

Pulatsu, B., Bretas, E.M., Lourenco, P.B., 2016. Discrete element modeling of masonry structures: Validation and application. Earthq. Struct. 11, 563–582.

Quezada, J.-C., Vincens, E., Mouterde, R., Morel, J.-C., 2016. 3D failure of a scale-down dry stone retaining wall : a DEM modelling. Eng. Struct. 117, 506–517.

Savalle, N., Vincens, E., Hans, S., 2018a. Pseudo-static scaled-down experiments on dry stone retaining walls: Preliminary implications for the seismic design. Eng. Struct. 171, 336–347. https://doi.org/10.1016/j.engstruct.2018.05.080

Savalle, N., Vincens, E., Hans, S., 2018b. SEISMIC BEHAVIOUR OF DRY STONE RETAINING WALLS: EXPERIMENTAL AND NUMERICAL PSEUDO-STATIC STUDIES. Presented at the International Masonry Conference, Milan, pp. 1030–1045.

Terrade, B., Colas, A.-S., Garnier, D., 2018. Upper bound limit analysis of masonry retaining walls using PIV velocity fields. Meccanica 53, 1661–1672.

Thew, I., Sutherland, A., Theodossopoulos, D., 2013. Structural response of drystone Iron Age brochs. Proc. Inst. Civ. Eng. - Struct. Build. 166, 316–324. https://doi.org/10.1680/stbu.11.00056

Villemus, B., Morel, J.-C., Boutin, C., 2006. Experimental assessment of dry stone retaining wall stability on a rigid foundation. Eng. Struct. 29, 2124–2132.

Walker, P., McCombie, P., Claxton, M., 2007. Plane strain numerical model for drystone retaining walls. Proc. Inst. Civ. Eng. - Geotech. Eng. 160, 97–103.

Walker, P.J., Dickens, J.G., 1995. Stability of medieval dry stone walls in Zimbabwe. Géotechnique 45, 141–147.

Zamiran, S., Osouli, A., 2018. Seismic motion response and fragility analyses of cantilever retaining walls with cohesive backfill. Soils Found. 58, 412–426. https://doi.org/10.1016/j.sandf.2018.02.010

I. Appendix: Assemblages used for walls with a high thickness

We present hereafter the geometrical properties of the bricks used in the experiments and in the simulations. We also give the assemblages used for walls of width B = 51mm (*Figure 18*); B = 68mm (*Figure 19*) and B = 85mm (*Figure 20*). Each layer of bricks corresponds to the height of bricks h = 11mm. All schemes were built to avoid any running joints on more than two layers on the internal and on the external faces. However, it was not possible to avoid all possible running joints inside the wall.
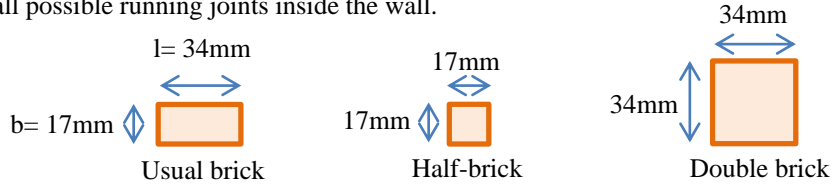

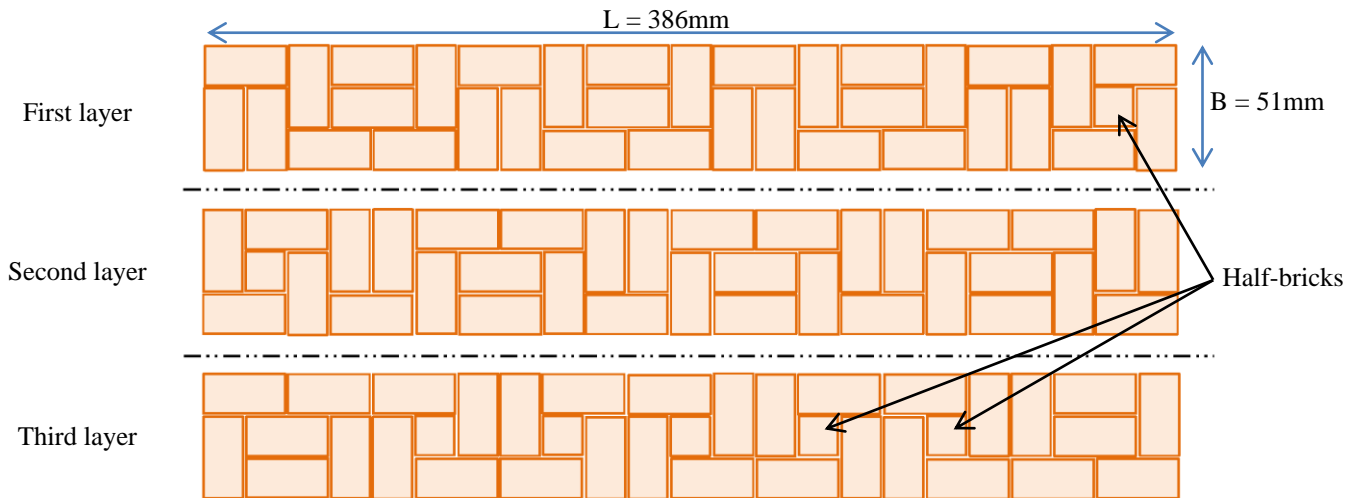*Figure 17: Dimensions of the bricks used to build the walls: top-view. They all had the same height: h = 11mm.*

Figure 18: Top-view of the assemblage used for the wall with B=51mm. The pattern that repeats in the vertical direction was composed of three brick layers. Then, the fourth layer repeated the assemblage of the first layer.

Figure 19: Top-view of the assemblage used for the wall with B=68mm. The pattern that repeats in the vertical direction was composed of three brick layers. Then, the fourth layer repeated the assemblage of the first layer.
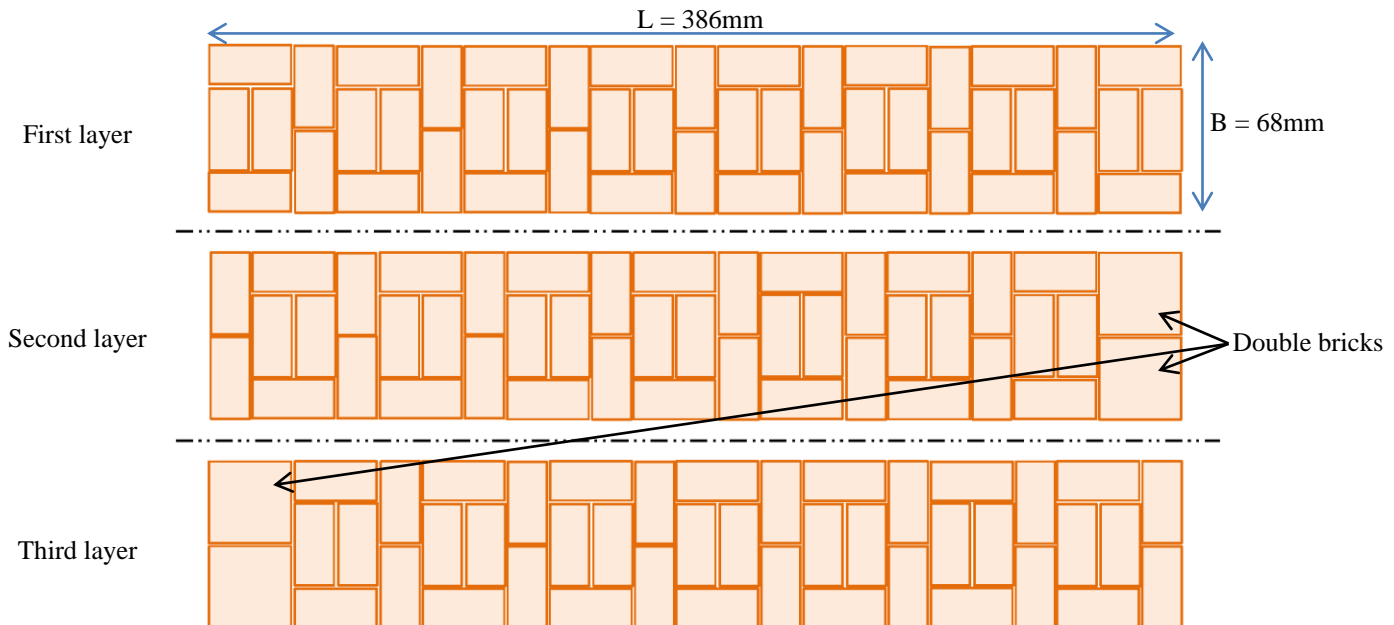
First layer

Second layer

Third layer

Fourth layer

Fifth layer

Sixth layer

Seventh layer

Eight layer

Ninth layer

Tenth layer

Eleventh layer
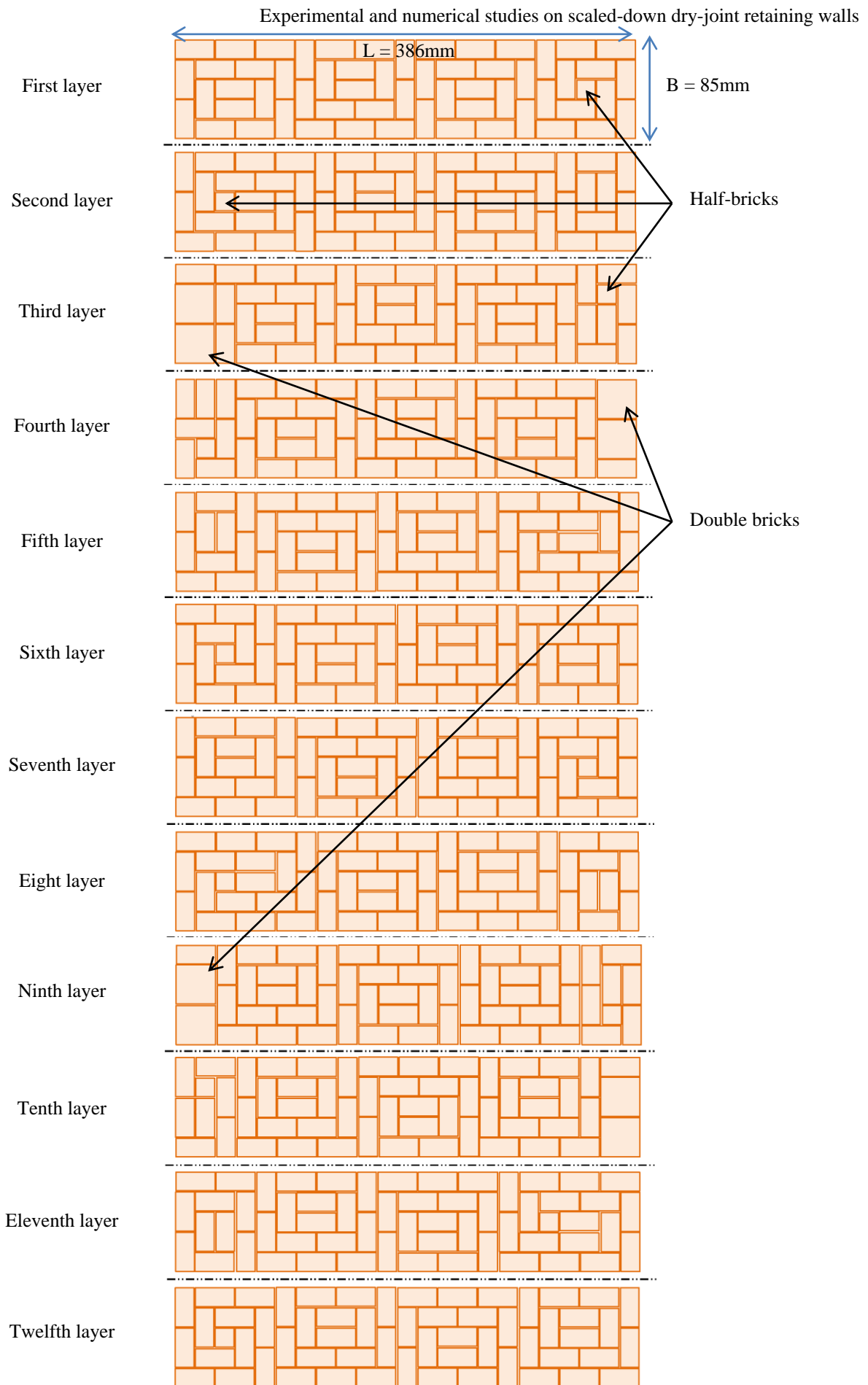
Twelfth layer

L = 386mm

B = 85mm

Half-bricks

Double bricks

Figure 20: Top-view of the assemblage used for the wall with B=85mm. The pattern that repeats in the vertical direction was composed of twelve brick layers. Then, the thirteenth layer repeated the assemblage of the first layer.

II.   Appendix: Computation of the energy of a retaining wall when falling

In this appendix, the approach to compute the kinetic energy of a retaining wall is developed. The goal is to define the energy thresholds for walls of different geometries knowing their value for a specific case (H_0, B_0). For the sake of simplicity, a case is presented to find a relevant approach to process it. One must note that this case is much simpler than the numerical model studied in the paper. However, the agreement of numerical and experimental results seems to show that this approach may be acceptable as a first estimate of these thresholds.

Using a simple equilibrium of a wall in the case of sliding failure, the equation of motion reads:

$$m\overrightarrow{a_g} = \sum \overrightarrow{F_{ext}}$$
$$m\overrightarrow{a_g} = \vec{P} + \overrightarrow{F_{earth}} + \vec{R}$$
$$m\overrightarrow{a_g} = [P\cos(\alpha) + F_{earth}\sin(\delta)]\vec{y} + [P\sin(\alpha) + F_{earth}\cos(\delta)]\vec{x} + \vec{R} \qquad (Eq.\ 5)$$

with m the mass of the wall, $\vec{P}$ the weight of the wall, $\overrightarrow{F_{earth}}$ the earth pressure, $\vec{R}$, the reaction of the foundation, α the inclination of the gravity, δ the inclination of earth pressure and $\vec{x}, \vec{y}$ the horizontal and vertical directions. Considering the wall sliding, at the limit equilibrium:

$$\vec{R} = -[P\cos(\alpha) + F_{earth}\sin(\delta)]\vec{y} - [P\cos(\alpha) + F_{earth}\sin(\delta)]\tan(\varphi)\vec{x}$$
$$\vec{R} = -[P\cos(\alpha) + F_{earth}\sin(\delta)]\vec{\varphi} \qquad (Eq.\ 6)$$

with $\vec{\varphi}$, the direction of the foundation soil reaction. Using the Coulomb's earth pressure coefficient K_a, *(Eq. 6)* becomes:

$$m\overrightarrow{a_g} = \gamma_{wall}HB \times \vec{g} + K_a \frac{\gamma_{soil}H^2}{2} \times \vec{\delta}$$
$$- \frac{1}{\cos(\varphi)}\left[\gamma_{wall}H_0 B_0 \times g\cos(\alpha) + K_a \frac{\gamma_{soil}H^2}{2}\sin(\delta)\right]\vec{\varphi} \qquad (Eq.\ 7)$$

where γ_{soil} and γ_{wall} are respectively the unit weight of the soil and of the wall, H the height of the wall and B, its width. The length of the wall has been ignored as computations were performed with a plane strain condition and as the stresses are identical in all the wall sections. The authors introduce the slenderness AR, defined as $AR = H/B$. Combining all these considerations and dividing by $m = \gamma_{wall}HB$, *(Eq. 7)* reads:

$$\overrightarrow{a_g} = \vec{g} + K_a \frac{AR \times \gamma_{soil}}{2 \times \gamma_{wall}} \times \vec{\delta} - \frac{1}{\cos(\varphi)}\left[g\cos(\alpha) + K_a \frac{AR \times \gamma_{soil}}{2 \times \gamma_{wall}}\sin(\delta)\right]\vec{\varphi} \qquad (Eq.\ 8)$$

Then, a statement is done where the dependence of *(Eq. 8)* with respect to the aspect ratio AR is neglected to allow simple and linear transpositions to other wall dimensions to be made[6]. Nevertheless, as the numerical method has been found in a good agreement with the experimental results whatever the aspect ratio of the wall, this choice seems to be acceptable as a preliminary approach.

Assuming that the acceleration ($\overrightarrow{a_g}$) does not depend on geometrical parameters, the velocity is not supposed to depend on geometrical parameters either. Then, calculating the kinetic energy (herein, only the translational part of the kinetic energy is given), it gives:

---

[6] In fact, another transposition method could be made neglecting the constant part of *(Eq. 8)*, keeping only the part dependent on the aspect ratio (AR).

$$E_c = \frac{1}{2} \times m \times |\vec{v}|^2$$
$$= \frac{1}{2} \times \gamma_{wall} HBL \times |\vec{v}|^2$$

<div align="right">(Eq. 9)</div>

where $|\vec{v}|$ is the velocity of the wall (assumed independent of the geometry of the wall) and L the length of the wall which is the same for all the walls studied herein. The kinetic energy is directly proportional to the height H and the width B of the wall. Therefore, the energy thresholds are also assumed to be directly proportional to the height H and the width B of the wall. For the particular case with $H_0 = 8.1 cm$ and $B_0 = 3.4 cm$, the thresholds were precisely defined and more generally, for a wall of height H and width B, the thresholds can be computed using the following Equations:

$$E_{c,min}(H,B) = \frac{H \times B}{H_0 \times B_0} \times E_{c,min}(H_0, B_0) = \frac{H \times B}{8.1 \times 3.4} \times 10^{-12} \qquad \text{(Eq. 10)}$$

$$E_{c,max}(H,B) = \frac{H \times B}{H_0 \times B_0} \times E_{c,max}(H_0, B_0) = \frac{H \times B}{8.1 \times 3.4} \times 10^{-10} \qquad \text{(Eq. 11)}$$

In addition, the same procedure can be followed considering the toppling mode of failure of the wall and the momentum equilibrium of the wall leading to the computation of the rotational kinetic energy of the wall.

III. Appendix: Parametric study involving the influence of the elastic properties of the materials

The elastic parameters of the wall-backfill system (bulk and shear modulus of the bricks, bulk and shear modulus of the backfill, stiffnesses of joints) were determined following either a previous study (Quezada et al., 2016) or UDEC manuals (e.g. classical values used for joint stiffnesses). This appendix aims at presenting a parametric study made on the basis of these elastic properties.

The stability of the tested retaining walls is supposed to depend on the strength of the materials (friction, cohesion, density). Therefore, the elastic properties are not expected to have an impact on the tilting angle at failure. We carried out an analysis of the impact of these elastic properties on the tilting angle at failure to confirm this statement.

The wall considered for the study is of height H = 81mm and width B = 34mm. The cross-section 1 (*Figure 1*) is considered. For that wall, the tilting angle at failure was 12.3° with the properties depicted in *Section 3*. The modulus of bricks (nominal value of E_{bricks} = 1 GPa), of the sand (nominal value of E_{sand} = 10 MPa) and the stiffness of the joints (nominal values for brick joint stiffnesses of $k_n = k_s$ =5000GPa/m and of $k_n = k_s$ = 100GPa/m for the sand joints) are studied. For the sake of simplicity only the brick stiffnesses are indicated in *Table 8* but the sand stiffnesses (and interface stiffnesses) are also decreased (or increased) proportionally. Despite the large (and yet unrealistic) range of variation of the elastic properties, the numerical results seem to be globally unchanged in terms of failure tilting angle α, confirming that the elastic properties of the materials do not have a significant impact on the stability of dry-joint retaining walls.

Table 8: Impact of the elastic properties of the materials and of the joints on the tilting angle at failure α. Bold values correspond to nominal values issued from the main study.

E_{bricks} (GPa)	α (°)	E_{sand} (MPa)	α (°)	Joint stiffness (GPa/m)	α (°)
0.001	11.1°	0.1	13.4°	1	12.6°
0.01	11.9°	0.5	12.4°	10	12.7°
0.05	11.9°	1	12.9°	50	12.7°
0.1	12.3°	2	12.3°	100	12.5°
0.2	13.2°	5	12.5°	500	12.1°
0.5	12.6°	**10**	**12.3°**	1000	12.3°
1	**12.3°**	20	12.3°	**5000**	**12.3°**